Journal of Hydro-environment Research 15 (2017) 13–26

Contents lists available at ScienceDirect

Journal of Hydro-environment Research

journal homepage: www.elsevier.com/locate/JHER

Research papers

Development of an upwinding kernel in SPH-SWEs model for 1D trans-critical open channel flows

Kao-Hua Chang [a,d], Tsang-Jung Chang [a,b,*], Tony Wen-Hann Sheu [c,d]

[a] Department of Bioenvironmental Systems Engineering, National Taiwan University, Taipei 106, Taiwan
[b] Hydrotech Research Institute, National Taiwan University, Taipei 106, Taiwan
[c] Center for Advanced Studies in Theoretical Sciences (CASTS), National Taiwan University, Taipei 106, Taiwan
[d] Department of Engineering Science and Ocean Engineering, National Taiwan University, Taipei 106, Taiwan

ARTICLE INFO

Article history:
Received 12 October 2015
Revised 8 December 2016
Accepted 5 January 2017
Available online 9 January 2017

Keywords:
Smoothed particle hydrodynamics
Open channel
Upwinding
Dispersion-relation-preserving

ABSTRACT

In this study, an upwinding SPH model with a non-symmetric kernel function is proposed to predict one-dimensional open channel flows. Due to the application of non-symmetric kernel function biased in favor of the upstream side, numerical diffusion is intrinsically added into the discretized momentum equation using SPH. The proposed model thus has shown to have good potential to resolve steep gradient or discontinuous solutions without the need of exactly adding artificial viscosity to the discretized equation. Furthermore, an upwinding coefficient for the determination of the degree of upwinding is derived to accommodate the dispersion-relation-preserving (DRP) property. In wave number space, the error between the discretized SPH equations and the original partial differential equations is minimized, thereby yielding the optimized upwinding coefficient. The proposed model has been validated by solving four benchmark problems involving non-rectangular cross section, varying channel width, non-uniform bed slope and hydraulic jump. Comparison of the numerical and exact solutions shows that the proposed model has the ability of accurately predicting various open channel flows involving complicated trans-critical flows. The consistency condition of the proposed model is also analyzed theoretically for the sake of completeness.

1. Introduction

Open channel flows commonly seen, for example, in river hydraulics (Szymkiewicz, 1991; Ying et al., 2004; Hsu et al., 2006; Chen et al., 2015), eco-hydrology (Jadhav and Buchberger, 1995; Anderson et al., 2006), and in hydrodynamics (Papanicolaou et al., 2004; Diaz et al., 2008) have been predicted by solving the shallow water equations (SWEs). Owing to the non-linear hyperbolic property in the shallow water equations, different wave propagation speeds in the flow allow steep gradient or discontinuous solutions to develop in the open channel flows subject to a rapidly deformed free surface. The resulting spurious oscillations in the vicinity of steep gradients and discontinuities will lead to divergent or unphysical solutions. To circumvent this problem, various discontinuity capturing mesh-based discretization methods have been developed over the past few decades. For instance, the MacCormack scheme (Garcia-Navarro and Saviron, 1992) and the Roe's approximate Riemann solver (Alcrudo et al., 1992) in finite difference method (FDM), the dissipative Galerkin scheme (Katopodes, 1984) in finite element method (FEM) and the total variation diminishing (TVD) scheme (Lin et al., 2003) in finite volume method (FVM) have been referred. These methods have been proven to be stable and accurate in the prediction of open channel flow problems containing sharply varying free surface.

In addition to the mesh-based methods, some meshless methods such as the smoothed particle hydrodynamics (SPH) (Liu and Liu, 2003; Monaghan, 2005; Gomez-Gesteira et al., 2010) have been recently applied to solve SWEs (the so-called SPH-SWEs model). Thanks to the Lagrangian nature, SPH method has the following advantages: (1) the mass conservation is satisfied; (2) the nonlinear convective term of SWEs is instinctively considered; and (3) the positive water depth is preserved by means of SPH summation operator even in a wet-dry interface. However, only few studies focused on the treatment of steep gradient or

* Corresponding author at: Department of Bioenvironmental Systems Engineering, National Taiwan University, Taipei 106, Taiwan.
E-mail addresses: f94622026@ntu.edu.tw (K.-H. Chang), tjchang@ntu.edu.tw (T.-J. Chang), twhsheu@ntu.edu.tw (T. Wen-Hann Sheu).

http://dx.doi.org/10.1016/j.jher.2017.01.001
1570-6443/

discontinuity in open channel flows have been reported. Wang and Shen (1999), Chang et al. (2011) and Kao and Chang (2012) used the Monaghan artificial viscosity formulation to investigate various dam-break flows, respectively. Ata and Soulaimani (2005) proposed a new artificial viscosity formulation based on the Lax-Friedrichs flux for the dam-break problem with wet bed. Chang and Chang (2013) utilized the artificial viscosity formulation of Lax-Friedrichs flux to study non-rectangular and non-prismatic open channel flows. Besides those, Vacondio et al. (2012b) introduced two-shock Riemann solver into the SPH-SWEs model to simulate oscillatory flows in a parabolic basin and the dam-break flows with dry bed.

In the literature, no SPH-SWEs model has exploited the non-symmetric kernel function to eliminate oscillations resulting from steep gradient or discontinuous solutions. Inspired by the works of Brooks and Hughes (1982) and Huang and Sheu (2012), we are led to learn that use of the upwinding technique can add more or less numerical diffusion into the flow direction to stabilize solutions. Hence, we are motivated to follow the same idea and propose in this study a new upwinding SPH kernel function and implement it to the SPH-SWEs model, namely the upwinding SPH-SWEs model, to resolve steep gradients or discontinuities in open channel flows. The upwinding SPH kernel function can be constructed by adding a weighted dissipation term to the symmetric SPH kernel functions such as the cubic spline kernel (Liu and Liu, 2003) and the Wendland kernel (Violeau, 2012). The use of the upwinding SPH kernel function which introduces damping mechanism to resolve steep gradient or discontinuous solutions results in a stabilized SPH-SWEs model. In addition, an upwinding coefficient, which determines the degree of upwinding, needs to be rigorously determined. The technique of spatial Fourier transform will be conducted to derive the numerical dispersion relation corresponding to the discretized SPH equations in wave number space. Both dispersion and dissipation errors resulting from the SPH discretization can be theoretically derived. The discretized SPH model is therefore subject to the satisfaction of the dispersion-relation-preserving (DRP) property (Tam and Webb, 1993; Cheong and Lee, 2001). The optimized upwinding coefficient thus derived can yield therefore the smallest dispersive and dissipative errors.

This paper is organized as follows. In Section 2 the model equations of shallow water including the variables of wetted cross-section area and water discharge are introduced. Section 3 presents the proposed upwinding SPH kernel function, the SPH operators and the upwinding SPH formulation. In Section 4 the consistency of the proposed model is analyzed theoretically. Finally, four benchmark cases featuring the non-rectangular cross section, varying channel width, non-uniform bed slope and hydraulic jump in open channel flows are solved to verify the proposed approach against the exact solutions in Section 5.

2. Shallow water equations

The model of SPH-SWEs governs water depth and water velocity in a rectangular or a prismatic open channel. The wetted cross-section area and the water discharge are introduced in the proposed SPH-SWEs model aiming at predicting non-rectangular and non-prismatic channel flows. The Lagrangian form of the SWEs expressed in terms of the wetted cross-section and the water discharge can be written as follows in Eq. (1) (continuity equation) and Eq. (2) (momentum equation)

$$\frac{\mathrm{D}A}{\mathrm{D}t} = -A\frac{\partial u}{\partial x}, \tag{1}$$

$$\frac{\mathrm{D}Q}{\mathrm{D}t} = -Q\frac{\partial u}{\partial x} - gA\frac{\partial d_w}{\partial x} + gA(S_0 - S_f). \tag{2}$$

In the above, $\frac{\mathrm{D}}{\mathrm{D}t}$ denotes the total time derivative term ($\frac{\mathrm{D}}{\mathrm{D}t} = \frac{\partial}{\partial t} + u\frac{\partial}{\partial x}$), Q is the water discharge, u is the water velocity (=Q/A), A is the wetted cross-section area, d_w is the water depth, S_0 is the bed slope, S_f is the friction slope (=$n^2Q^2/A^2R4/3$), n is the Manning roughness coefficient, R is the hydraulic radius, and g is the gravitational acceleration.

3. Upwinding SPH model

Any physical quantity at particle a (ϕ_a) can be approximated as follows within the SPH context.

$$\phi_a = \int \phi(x)\omega(x_a - x, h)\mathrm{d}V \cong \sum_{b=1}^{b=N} m_b \frac{\phi_b}{A_b}\omega(r_{ab}, h_a) \tag{3}$$

In the above, m_b (= $A_bV_b = A_b\Delta x_0$) is the mass of particle b, V_b (= Δx_0 at the initial state) is the volume of particle b, A_b is the wetted cross-section area of particle b, Δx_0 is the initial particle spacing, x is the position of a particle, r_{ab} (= $|x_a - x_b|$) is the distance between particles a and b, $\omega(r_{ab}, h_a)$ is the symmetric kernel function of particle a. In this study, h_a denotes the smoothing length of particle a (=1.2 Δx_0) and N is the particle number in the support domain of particle a (=5 in this study due to the smoothing length being set at 1.2 Δx_0).

The standard SPH operator for the first derivative of a physical quantity at particle a is shown below

$$\left(\frac{\partial \phi}{\partial x}\right)_a = -\int \phi(x)\frac{\partial \omega(|x_a - x|, h)}{\partial x}\mathrm{d}x \cong -\sum_{b=1}^{b=N}\frac{m_b}{A_b}\phi_b\frac{\partial \omega(r_{ab}, h_a)}{\partial x_b} \tag{4}$$

Note that Eq. (4) cannot properly approximate the first derivative in the sense that the first derivative vanishes, if the physical quantity is constatnt. Therefore, an alternative SPH operator for the first derivative of a physical quantity at particle a is adopted as follows (Chang and Chang, 2013):

$$\left(\frac{\partial \phi}{\partial x}\right)_a = \frac{1}{A_a}\sum_{b=1}^{b=N} m_b(\phi_a - \phi_b)\frac{\partial \omega(r_{ab}, h_a)}{\partial x_b} \tag{5}$$

It is addressed that Eq. (5) is symmetric with respect to a and b.

3.1. Development of new upwinding kernel function

In this study, an upwinding kernel function (W) will be derived with an aim to resolve oscillations near steep gradient or discontinuous solutions. Our strategy is to modify the symmetric kernel function (ω) by adding a dissipative term (ΔD), thereby leading to

$$W(r_{ab}, h_a) = \omega(r_{ab}, h_a) + \Delta D \tag{6}$$

Hereafter, we denote $W(r_{ab}, h_a)$ as W^a_{ab}, $\omega(r_{ab}, h_a)$ as ω^a_{ab}, $\frac{\partial W(r_{ab}, h_a)}{\partial x_b}$ as $W^a_{ab,x}$ and $\frac{\partial \omega(r_{ab}, h_a)}{\partial x_b}$ as $\omega^a_{ab,x}$.

The following modified dissipative term for particle a has the form similar to that used by Brooks and Hughes (1982) and Huang and Sheu (2012).

$$\Delta D = \tau_a u_a \omega^a_{ab,x} \tag{7}$$

In ΔD, τ_a denotes the upwinding coefficient of particle a and determines the degree of upwinding and u_a is the velocity of particle a. The upwinding kernel function for particle a is therefore written as

$$W^a_{ab} = \omega^a_{ab} + \tau_a u_a \omega^a_{ab,x} \tag{8}$$

In the proposed SPH-SWEs model, the upwinding coefficient (τ) which has a great impact on the numerically introduced dispersive and dissipative errors needs to be rigorously derived. Firstly, SPH approximates the first derivative of particle a as

$$\left(\frac{\partial u}{\partial x}\right)_a = \frac{1}{A_a}\sum_{b=1}^{b=N} m_b(u_a - u_b)W^a_{ab,x}. \tag{9}$$

By applying the differential operator on Eq. (8) and substituting it into Eq. (9), we can get

$$\left(\frac{\partial u}{\partial x}\right)_a = \frac{1}{A_a}\sum_{b=1}^{b=N} m_b(u_a - u_b)(\omega^a_{ab,x} + \tau_a u_a \omega^a_{ab,xx}) \tag{10}$$

Eq. (10) can be further rewritten to the following equation:

$$\left(\frac{\partial u}{\partial x}\right)_a = \sum_{b=1}^{b=N} f_b u_b \tag{11}$$

where $f_b = -m_b(\omega^a_{ab,x} + \tau_a n u_a \omega^a_{ab,xx})/A_a$ when $b \neq a$ and $f_a = -\sum_{b=1}^{b=N, b\neq a} f_b$.

We then perform Fourier transform on Eq. (11) (Tam and Webb, 1993; Li, 1997), leading to

$$i\alpha\tilde{u} = \left(\sum_{b=1}^{b=N} f_b e^{i\alpha l_b \Delta}\right)\tilde{u} \tag{12}$$

where $\tilde{u}$ is the Fourier transform of velocity u, α is the exact wave number,

$$\Delta = \frac{|x_1 - x_N|}{N-1}, l_b = \frac{x_b - x_a}{\Delta} \quad \text{and} \quad i = \sqrt{-1}$$

By comparing both sides of Eq. (12), the numerical wave number ($\hat{\alpha}$) can be derived as

$$\hat{\alpha} = -i\sum_{b=1}^{b=N} f_b e^{i\alpha l_b \Delta} = \hat{\alpha}_r - i\hat{\alpha}_i. \tag{13}$$

Note that $\hat{\alpha}_r$ denotes the real part of the numerical wave number $\left(=\sum_{b=1}^{b=N, b\neq a} f_b \sin(\alpha l_b \Delta)\right)$ and $\hat{\alpha}_i$ is the imaginary part of the numerical wave number $\left(=\sum_{b=1}^{b=N} f_b \cos(\alpha l_b \Delta)\right)$ (Li, 1997).

Following the work of Tam and Webb (1993) and Cheong and Lee (2001), the difference between the exact and numerical wave numbers is defined as

$$E = E_r + E_i = \int_0^{\pi/2} |k_r - k|^2 \mathrm{d}k + \lambda \int_0^{\pi/2} \left| k_i - e^{-\ln 2\cdot\left(\frac{k-\pi}{\sigma}\right)^2} \right|^2 \mathrm{d}k \tag{14}$$

where E_r and E_i are the differences between the real parts and the imaginary parts of the exact and numerical wave numbers, respectively, $k = \alpha\Delta$, $k_r = \hat{\alpha}_r\Delta$, $k_i = \hat{\alpha}_i\Delta$, λ is the weighted parameter whose performance is assessed in Appendix B (=1 in this study) and σ is the half-width of Gaussian function (=0.4π in this study).

The value of E is a minimum provided that

$$\frac{\partial E}{\partial f_{ct}} = 0 \quad ct = 1, N \quad \text{but} \quad ct \neq a \tag{15}$$

Herein, the upwinding coefficient can be derived as Eq. (16) and the derivation detail is given in Appendix A.

$$\tau_a = \frac{1}{u_a}\frac{-\sum_{b=1}^{b=N} m_b(C_b - C_a)\omega^a_{ab,x} + A_a(S_r + \lambda S_i)}{\sum_{b=1}^{b=N} m_b(C_b - C_a)\omega^a_{ab,xx}} \tag{16}$$

where $C_a = \lambda\Delta\left[\frac{\sin((l_a - l_{ct})\pi/2)}{l_a - l_{ct}} + \frac{\sin((l_a + l_{ct})\pi/2)}{l_a + l_{ct}}\right]$,

$$C_b = \Delta\left[(\lambda+1)\frac{\sin((l_b - l_{ct})\pi/2)}{l_b - l_{ct}} + (\lambda-1)\frac{\sin((l_b + l_{ct})\pi/2)}{l_b + l_{ct}}\right],$$

$$S_r = -2\int_0^{\pi/2} k\sin(l_{ct}k)\mathrm{d}k,$$

$$S_i = -2\int_0^{\pi/2} \cos(l_{ct}k)\cdot e^{-\ln 2\cdot\left(\frac{k-\pi}{\sigma}\right)^2}\mathrm{d}k, \quad \text{and} \quad \frac{\partial^2\omega(r_{ab}, h_a)}{\partial x_b^2} \text{ denotes } \omega^a_{ab,xx}.$$

Substituting Eq. (16) into Eq. (8), the upwinding kernel function can be finally expressed as

$$W^a_{ab} = \omega^a_{ab} + \frac{-\sum_{b=1}^{b=N} m_b(C_b - C_a)\omega^a_{ab,x} + A_a(S_r + \lambda S_i)}{\sum_{b=1}^{b=N} m_b(C_b - C_a)\omega^a_{ab,xx}}\omega^a_{ab,x} \tag{17}$$

3.2. Evaluation of the wetted cross-section area

Commonly, two numerical approaches can be applied to calculate the wetted cross-section area in SPH-SWEs. One can achieve the goal either through the continuity equation (1) or by virtue of the SPH summation operator shown in Eq. (3). To avoid a negative wetted cross-section area, the proposed model adopts the latter approach to compute the wetted cross-section area of each particle a. Since the smoothing length is allowed to vary for getting a more accurate SWEs solution, the smoothing length of particle a is connected to the wetted cross-section area (Chang and Chang, 2013; Rodriguez-Paz and Bonet, 2005) by virtue of

$$h_a = h_{0,a}\left(\frac{A_{0,a}}{A_a}\right)^{1/D_m} \tag{18}$$

In the above, A_{0_a} and h_{0_a} are the initial wetted cross-section area and the smoothing length for particle a, respectively, and D_m is the number of space dimensions ($D_m = 1$ in this study).

Because of the variable smoothing length, the Newton-Raphson iterative method is performed to solve the wetted cross-section area of particle a. The iterative procedure (Chang and Chang, 2013; Rodriguez-Paz and Bonet, 2005) is as follows:

$$A_a^{k+1} = A_a^k\left[1 - \frac{\mathrm{Res}_a^k D_m}{(\mathrm{Res}_a^k D_m + \alpha_a^k)}\right] \tag{19}$$

with

$$\mathrm{Res}_a^k = A_a^k - \sum_{b=1}^{b=N} m_b\omega^a_{ab} \tag{20}$$

where Res_a^k is the residual of particle a at the kth iteration and α_a^k is defined as

$$\alpha_a^k = -\sum_b m_b r_{ab}\frac{d\omega^a_{ab}}{dr} \tag{21}$$

Application of the Newton-Raphson iterative procedure will be terminated provided that

$$\frac{\mathrm{Res}_a^{k+1}}{A_a^k} \leqslant 10^{-10} \tag{22}$$

Moreover, as the problems with steep gradient or discontinuous bottom profiles are encountered, a balance correction in calculating the water depths proposed by Vacondio et al. (2013) and Xia et al. (2013) is commonly used to improve unphysical oscillation in water depth.

3.3. Approximation of momentum equation

The discretized SPH form of the momentum equation [Eq. (2)] is derived next to evaluate the rate of water discharge of each particle a

$$\left(\frac{DQ}{Dt}\right)_a = -u_a\sum_{b=1}^{b=N} m_b(u_a-u_b)\overline{W_x} - g\sum_{b=1}^{b=N} m_b(d_{w,a}-d_{w,b})\overline{\omega_x} + gA_a(S_{0,a}-S_{f,a}) \quad (23)$$

where $\bar{W}_x = \bar{\omega}_x + \bar{\tau}\bar{\omega}_{xx}$. Due to the varied smoothing length, we express $\bar{\omega}x = 0.5\cdot(\omega^a_{ab,x}+\omega^b_{ab,x})$, $\bar{\omega}_{xx} = 0.5\cdot(\omega^a_{ab,xx}+\omega^b_{ab,xx})$, and $\bar{\tau} = 0.5\cdot(\tau_a u_a + \tau_b u_b)$ (Hernquist and Katz, 1989).

As to the bed slope term S_{0_a} shown on the right hand side of Eq. (23), virtual bed particles are introduced to calculate the bed slope of particle *a* (Chang and Chang, 2013; Vacondio et al., 2012a). Fig. 1 shows the schematic of the computational domain. In this study, the computational domain is divided into three zones, *i.e.* the inflow zone (the zone between the inlet boundary and the inflow boundary), the fluid zone (the zone between the inflow boundary and the outflow boundary), and the outflow zone (the zone between the outflow boundary and the outlet boundary). In addition, four particle types are used, including the inflow particles, inner particles, outflow particles and virtual bed particles (*i.e.* rectangular points, circle points, diamond points and triangular points, respectively, shown in Fig. 1). The former three types correspond respectively to the flow zone, the fluid zone and the outflow zone. The last type is the computational domain.

Each virtual bed particle has a specified value of the bed slope and its volume equals Δx_0. Then, the bed slope of the inflow/inner/outflow particle *a* is computed by incorporating the bed slope of each virtual bed particle surrounding the inflow/ inner/ outflow particle *a* into the SPH summation operator as shown below

$$S_{0,a} = \sum_{b=1,b\in vb}^{b=N} V_b S_{0,b}\tilde{\omega}^b_{ab} \quad (24)$$

Here, the notation $\tilde{\omega}^b_{ab}$ denotes the corrected kernel function as (Randles and Libersky, 1996)

$$\tilde{\omega}^b_{ab} = \frac{\omega^b_{ab}}{\sum_{b=1,b\in vb}^{b=N} V_b\omega^b_{ab}} \quad (25)$$

where the subscript *vb* denotes the virtual bed particle and $h_{b\in vb}) = 1.2\Delta x_0$.

3.4. In/out-flow boundary conditions

Four kinds of boundary conditions can be specified according to the local flow conditions (or Froude number) at the in/out-flow boundaries. In the treatment of the in/out-flow boundary conditions, the specified time interval method (Sturm, 2010) is adopted to compute the unknown variables at in/out-flow boundaries along the negative and positive characteristic lines *LP* and *RS* schematic in Fig. 2 for every time step. As the subcritical flow occurs at the inflow boundary (Line *LP* in Fig. 2), the water discharge is prescribed and the water depth is calculated by solving Eq. (26) iteratively through the Newton-Raphson iteration procedure.

$$Q_p = A_P\left[u_L + \frac{g}{c_L}(d_{w,P}-d_{w,L}) + g(S_{0,L}-S_{f,L})\Delta t\right] \quad (26)$$

As the subcritical flow occurs at the outflow boundary (Line *RS* in Fig. 2), the water depth is prescribed and the water discharge is determined from Eq. (27).

$$Q_S = A_S\left[u_R - \frac{g}{c_R}(d_{w,S}-d_{w,R}) + g(S_{0,R}-S_{f,R})\Delta t\right] \quad (27)$$

The values of all physical variables at points *L* and *R* are determined by the specified time interval method. For greater details on this method, one can refer to Federico et al. (2012), Chang and Chang (2013) and Aristodemo et al. (2015).

Provided that the supercritical flow occurs at the inflow boundary, the water depth and the water discharge are prescribed, while the water depth and the water discharge are not necessarily to be specified as those of the supercritical flow at the outflow boundary.

3.5. Time integration scheme

The leap-frog time integration scheme (Bonet and Lok, 1999) which can conserve linear and angular momentum exactly is used to update the particle positions and discharge in time, *i.e.*, Eqs. (28) to (30).

$$Q_a^{n+1/2} = Q_a^{n-1/2} + \Delta t\left(\frac{dQ}{dt}\right)_a^n \quad (28)$$

$$x_a^{n+1} = x_a^n + \Delta t A_a^n Q_a^{n+1/2} \quad (29)$$

$$Q_a^{n+1} = Q_a^{n+1/2} + 0.5\Delta t\left(\frac{dQ}{dt}\right)_a^n \quad (30)$$

Due to the fact that SPH is an explicit method, the chosen time step (Δt) has to satisfy the CFL condition given below

$$\Delta t \leqslant N_{CFL}\cdot\min\left(\frac{\Delta x_0}{u_a+\sqrt{gH_{d,a}}}\right) \quad (31)$$

where H_d is the hydraulic depth and N_{CFL} is set to 0.4.

4. Fundamental studies on the proposed SPH model

4.1. Upwinding kernel function

In this study, the Wendland kernel (Violeau, 2012), or Eq. (32), is adopted to be a symmetric kernel function to establish an upwinding kernel function. The first and second derivatives of the Wendland function are described below

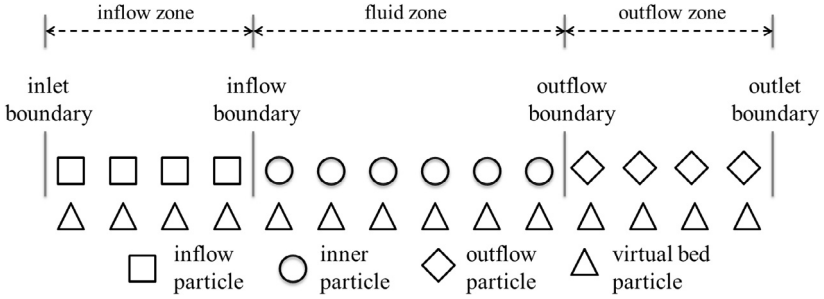

Fig. 1. Schematic of the investigated computational domain.

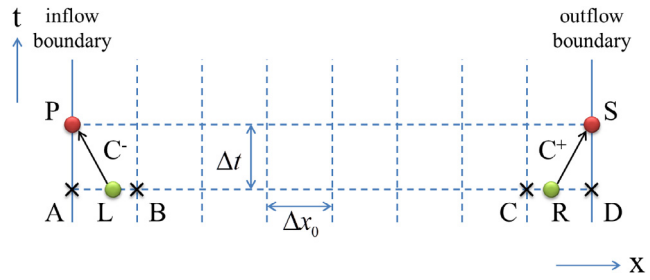

Fig. 2. Schematic of the in/out-flow boundary conditions.

$$\omega(s,h)=\frac{3}{4h}\begin{cases}(1+2s)\left(1-\frac{s}{2}\right)^4 & 0\leqslant s\leqslant 2\\ 0 & s>2\end{cases} \tag{32}$$

$$\frac{\partial\omega(s,h)}{\partial s}=\frac{3}{4h}\begin{cases}-5s\left(1-\frac{s}{2}\right)^3 & 0\leqslant s\leqslant 2\\ 0 & s>2\end{cases} \tag{33}$$

$$\frac{\partial^2\omega(s,h)}{\partial s^2}=\frac{3}{4h}\begin{cases}5(-1+2s)\left(1-\frac{s}{2}\right)^2 & 0\leqslant s\leqslant 2\\ 0 & s>2\end{cases} \tag{34}$$

where $s=r/h$.

Here, the property of the integrals of the upwinding kernel function and its first derivative are investigated. For particle a, the support domain in one dimension lies between two points x_a-2h_a and x_a+2h_a. Eq. (35) shows that the integral of W^a_{ab} can be divided into two terms including the integrals of ω^a_{ab} and $\omega^a_{ab,x}$, respectively. Besides, Eq. (36), which shows the integral of $W^a_{ab,x}$, can also be divided into two terms including the integrals of $\omega^a_{ab,x}$ and $\omega^a_{ab,xx}$, respectively. Hence, it can be shown that the integral of the upwinding kernel function in the support domain is 1 while the integral of its first derivative in the support domain is 0.

$$\begin{aligned}\int_{x_a-2h_a}^{x_a+2h_a}W^a_{ab}\mathrm{d}x_b&=\int_{x_a-2h_a}^{x_a+2h_a}(\omega^a_{ab}+\tau_a u_a\omega^a_{ab,x})\mathrm{d}x_b\\&=\int_{x_a-2h_a}^{x_a+2h_a}\omega^a_{ab}\mathrm{d}x_b+\tau_a u_a\int_{x_a-2h_a}^{x_a+2h_a}\omega^a_{ab,x}\mathrm{d}x_b=1\end{aligned} \tag{35}$$

$$\begin{aligned}\int_{x_a-2h_a}^{x_a+2h_a}W^a_{ab,x}\mathrm{d}x_b&=\int_{x_a-2h_a}^{x_a+2h_a}(\omega^a_{ab,x}+\tau_a u_a\omega^a_{ab,xx})\mathrm{d}x_b\\&=\int_{x_a-2h_a}^{x_a+2h_a}\omega^a_{ab,x}\mathrm{d}x_b+\tau_a u_a\int_{x_a-2h_a}^{x_a+2h_a}\omega^a_{ab,xx}\mathrm{d}x_b=0\end{aligned} \tag{36}$$

Assuming that the velocity of particle a is equal to 1, the upwinding kernel function and its first derivative under uniform particle spacings are depicted in Fig. 3. In contrast to the symmetric kernel functions such as Gaussian function (Liu and Liu, 2003), cubic function (Liu and Liu, 2003) and Wendland function shown in Fig. 3a, the upwinding kernel function has a larger weight at the upstream side than that at the downstream side. In addition, Fig. 3b gives the first derivatives of the four kernel functions. To compare with the three symmetric kernel functions, the proposed upwinding kernel function has larger gradient of the first derivative in the vicinity of $x_{ba}=0$. The gradient directions at the upstream and downstream sides of $x_{ba}=0$ are opposite for the proposed kernel function while the gradient directions at the upstream and downstream sides of $x_{ba}=0$ are identical for the three symmetric kernel functions.

4.2. Numerical wavenumber

In this section, the performance of numerical wavenumbers will be discussed under the circumstance of uniform particle sizes. Considering the velocity of a particle as 1, the real part and imaginary parts of the numerical wavenumber are presented in Fig. 4. In Fig. 4a, we can find that the numerical wavenumbers are nearly the same as the exact ones as $\alpha\triangle$ becomes smaller than 0.4. This means that the proposed model is adequate to resolve waves with a wave length larger than the 16 uniform particle spacing. Moreover, Fig. 4b shows that the numerical dissipation given by the proposed model increases as the wavenumber increases. Since the Gaussian function peak occurs at $\alpha\triangle=\pi$ and decays quickly towards the long wave components, the numerical dissipation is large for short wave components and its maximum is $\alpha\triangle=\pi$ while the numerical dissipation is small for the long wave components.

4.3. Scheme consistency

4.3.1. Consistency in space

Following the work of Quinlan et al. (2006) in studying the spatial consistency, the integral approximation of the first derivative of a physical quantity of particle a such as Eq. (37) is used herein.

$$\left(\frac{\partial\phi}{\partial x}\right)_a\cong-\int_{x_a-2h_a}^{x_a+2h_a}\phi_b W^a_{ab,x}\mathrm{d}x_b \tag{37}$$

In Eq. (37), ϕ_b can be expanded in Taylor series about x_a, *i.e.*, Eq. (38). Then, Eq. (37) can be written as Eq. (39).

$$\phi_b=\phi_a+\Delta x\left(\frac{\partial\phi}{\partial x}\right)_a+\frac{\Delta x^2}{2!}\left(\frac{\partial^2\phi}{\partial x^2}\right)_a+\frac{\Delta x^3}{3!}\left(\frac{\partial^3\phi}{\partial x^3}\right)_a+\cdots \tag{38}$$

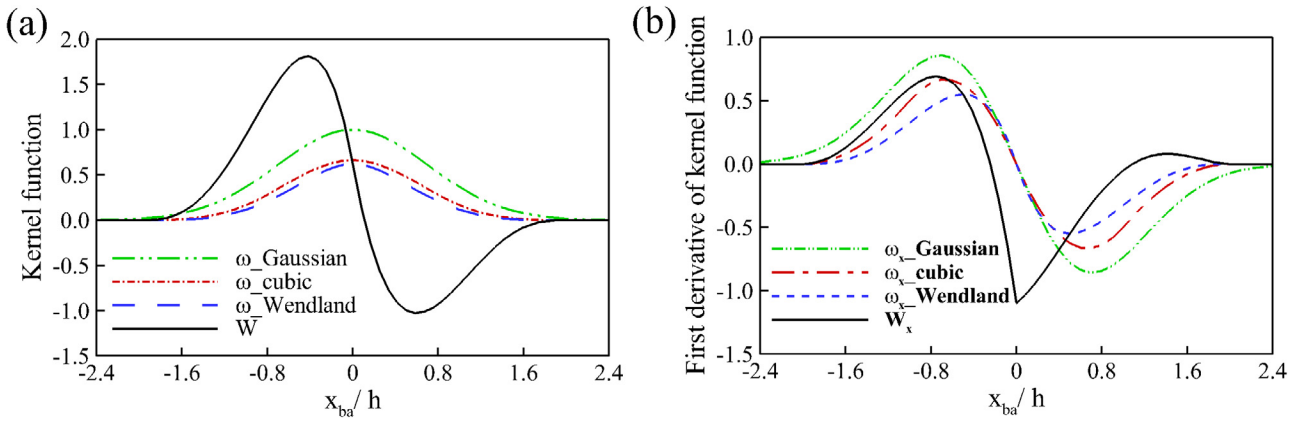

Fig. 3. The plots of (a) the upwinding kernel function and (b) its first derivative.

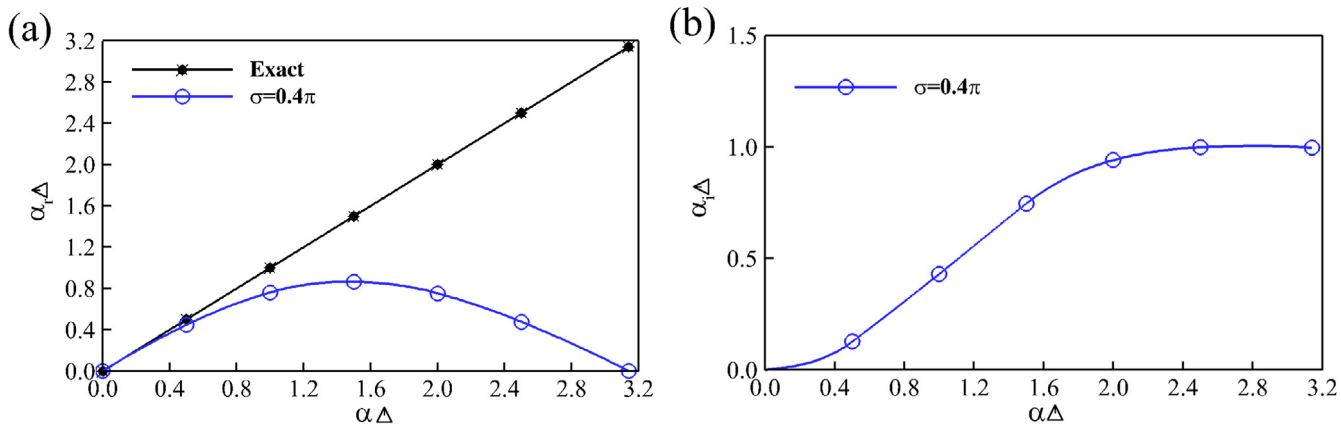

Fig. 4. Numerical wavenumber. (a) real part; (b) imaginary part.

$$\left(\frac{\partial\phi}{\partial x}\right)_a \cong -\phi_a\int_{x_a-2h}^{x_a+2h_a} W^a_{ab,x}\mathrm{d}x_b - \left(\frac{\partial\phi}{\partial x}\right)_a\int_{x_a-2h}^{x_a+2h_a}\Delta x W^a_{ab,x}\mathrm{d}x_b - \left(\frac{\partial^2\phi}{\partial x^2}\right)_a\int_{x_a-2h_a}^{x_a+2h_a}\frac{\Delta x^2}{2!}W^a_{ab,x}\mathrm{d}x_b - \left(\frac{\partial^3\phi}{\partial x^3}\right)_a \times\int_{x_a-2h_a}^{x_a+2h_a}\frac{\Delta x^3}{3!}W^a_{ab,x}\mathrm{d}x_b - \cdots \tag{39}$$

where $\Delta x = x_b - x_a$.

By virtue of Eq. (8) and the integration by parts, we can have

$$\int_{x_a-2h}^{x_a+2h_a}\Delta x W^a_{ab,x}\mathrm{d}x_b = \int_{x_a-2h}^{x_a+2h_a}\Delta x(\omega^a_{ab,x}+\tau_a u_a\omega^a_{ab,xx})\mathrm{d}x_b = -1 \tag{40}$$

$$\int_{x_a-2h_a}^{x_a+2h_a}\frac{\Delta x^2}{2!}W^a_{ab,x}\mathrm{d}x_b = \int_{x_a-2h_a}^{x_a+2h_a}\frac{\Delta x^2}{2!}(\omega^a_{ab,x}+\tau_a u_a\omega^a_{ab,xx})\mathrm{d}x_b = \tau_a u_a \tag{41}$$

$$\int_{x_a-2h_a}^{x_a+2h_a}\frac{\Delta x^3}{3!}W^a_{ab,x}\mathrm{d}x_b = \int_{x_a-2h_a}^{x_a+2h_a}\frac{\Delta x^3}{3!}(\omega^a_{ab,x}+\tau_a n u_a\omega^a_{ab,xx})\mathrm{d}x_b = -\frac{1}{2}\int_{x_a-2h_a}^{x_a+2h_a}\Delta x^2\omega^a_{ab}\mathrm{d}x_b \tag{42}$$

By substituting Eqs. (36), (40), (41) and (42) into Eq. (39), the integral approximation of $(\partial\phi/\partial x)_a$ becomes

$$\left(\frac{\partial\phi}{\partial x}\right)_a \cong \left(\frac{\partial\phi}{\partial x}\right)_a - \tau_a n u_a\left(\frac{\partial^2\phi}{\partial x^2}\right)_a + \frac{1}{2}\left(\frac{\partial^3\phi}{\partial x^3}\right)_a \times\int_{x_a-2h_a}^{x_a+2h_a}\Delta x^2\omega^a_{ab}\mathrm{d}x_b + \cdots \tag{43}$$

Definitions of $s = \frac{\Delta x}{h_a}$ and $\hat{\omega} = h_a\omega^a_{ab}$ give all kernel integrals of Eq. (43) in the non-dimensional forms as

$$\left(\frac{\partial\phi}{\partial x}\right)_a \cong \left(\frac{\partial\phi}{\partial x}\right)_a - \tau_a n u_a\left(\frac{\partial^2\phi}{\partial x^2}\right)_a + \frac{h^2}{2}\left(\frac{\partial^3\phi}{\partial x^3}\right)_a\int_{-2}^{2}s^2\hat{\omega}\mathrm{d}s + \cdots = \left(\frac{\partial\phi}{\partial x}\right)_a - \tau_a u_a\left(\frac{\partial^2\phi}{\partial x^2}\right)_a + O(h^2) \tag{44}$$

Eq. (44) shows that the kernel integrals only depend on the dimensionless shape of a kernel function in each problem with all length scales. From Eq. (44), we are led to know that the error of the integral approximation of the first spatial derivative resulting from the proposed model is $O(h^2)$ in addition to the numerical diffusion term $(-\tau_a u_a(\partial^2\phi/\partial x^2)_a)$.

4.3.2. Consistency in time

For showing the consistency in time in the proposed model, $Q_a^{n+1/2}$ is firstly expanded in Taylor series about Q_a^n, leading to

$$Q_a^{n+1/2} = Q_a^n + 0.5\Delta t\left(\frac{\mathrm{d}Q}{\mathrm{d}t}\right)_a^n + O(\Delta t^2) \tag{45}$$

Then, Eq. (46) can be obtained by substituting Eq. (45) into Eq. (30). It can be realized that the proposed model has the discretized error in time of the order $O(\Delta t^2)$.

$$Q_a^{n+1} = Q_a^n + \Delta t\left(\frac{\mathrm{d}Q}{\mathrm{d}t}\right)_a^n + O(\Delta t^2) \tag{46}$$

5. Results and discussion

In this section, four benchmark study cases given by MacDonald et al. (1995) are used to verify the newly proposed upwinding SPH-SWEs approach. The channel slope and the exact solution of water depth for each case can be seen in Appendix C. Four combinations of the in/out-flow boundary conditions, including subcritical inflow to supercritical outflow, subcritical inflow to subcritical outflow, supercritical inflow to supercritical outflow and supercritical inflow to subcritical outflow are respectively considered in the four study cases. These four cases involve rectangular and trapezoidal channels, uniform and non-uniform widths, non-uniform bed slope, transcritical flow and hydraulic jump. In this study, the major cause for the occurrence of a hydraulic jump is the variation of bed elevation instead of in/out-flow boundary conditions, which are the minor cause. Hence, the Froude numbers at the upstream and downstream sides in the vicinity of a hydraulic jump govern the behavior of the hydraulic jump occurring in each case. Table 1 shows the Froude numbers of all the study cases. According to the classification of hydraulic jump (Federico et al., 2012), the type of hydraulic jumps formed in all the cases is undular, which is characterized by undulations of the water surface without vortex dynamics on the crests. Furthermore, the spatial and temporal convergences and the accuracy of the proposed model are discussed in every study case. All the numerical simulations are performed on an Intel(R) Core(TM) i7-2600 CPU 3.4 GHz PC equipped with a 4 GB RAM.

The spatial and temporal convergence analyses are conducted using the simulated results of different resolutions in space and in time, respectively. Herein, the spatial and the temporal absolute errors $E_s^{\Delta x_{0,1},\Delta x_{0,2}}$ and $E_t^{\Delta t_1,\Delta t_2}$ obtained on the basis of the water discharge between the simulated results of two initial particle sizes

Table 1
The Froude numbers at the upstream and downstream sides in the vicinity of a hydraulic jump in each study case.

Case	Location	
	Upstream side	Downstream side
1	1.27	0.57
2	1.28	0.38
3	1.59	0.65
4	1.24	0.54

Table 2
The required CPU times of each study case between the upwinding and standard SPH-SWEs models.

Case	Model	
	Upwinding SPH-SWEs	Standard SPH-SWEs
1 ($\Delta x_0 = 5$ m,$\Delta t = 0.20$ s)	11.638 s	5.710 s
2 ($\Delta x_0 = 5$ m,$\Delta t = 0.20$ s)	19.001 s	9.766 s
3 ($\Delta x_0 = 5$ m,$\Delta t = 0.20$ s)	11.076 s	5.226 s
4 ($\Delta x_0 = 5$ m,$\Delta t = 0.16$ s)	13.931 s	6.474 s

of $\Delta x_{0,1}$ and $\Delta x_{0,2}$ and two time steps of Δt_1 and Δt_2 are defined as Eqs. (47) and (48), respectively.

$$E_s^{\Delta x_{0,1},\Delta x_{0,2}} = \sum_{i=1}^{i=N_g} |Q_i^{\Delta x_{0,1}} - Q_i^{\Delta x_{0,2}}| \tag{47}$$

$$E_t^{\Delta t_1,\Delta t_2} = \sum_{i=1}^{i=N_g} |Q_i^{\Delta t_1} - Q_i^{\Delta t_2}| \tag{48}$$

where N_g is the number of fixed grids.

Assuming that the spatial and temporal absolute errors are respectively proportional to the initial particle spacing and the time step (Ogami, 1999; Shao and Lo, 2003), the spatial and temporal absolute errors can also be rewritten as Eqs. (49) and (50), respectively.

$$E_{r,s}^{\Delta x_{0,1},\Delta x_{0,2}} = k_s(\Delta x_{0,1})^{SCOV} - k_s(\Delta x_{0,2})^{SCOV} \tag{49}$$

$$E_{r,t}^{\Delta t_1,\Delta t_2} = k_t(\Delta t_1)^{TCOV} - k_t(\Delta t_2)^{TCOV} \tag{50}$$

where *SCOV* and *TCOV* are the spatial and temporal convergence rates, respectively, and k_s and k_t are two constants.

Three initial particle sizes of $\Delta x_{0,1}$, $\Delta x_{0,2}(=\beta\Delta x_{0,1})$ and $\Delta x_{0,3}(=\beta^2\Delta x_{0,1})$ and three time steps of Δt_1, $\Delta t_2(=\beta\Delta t_1)$ and $\Delta t_3(=\beta^2\Delta t_1)$, where β is a constant, are involved in the evaluation of the spatial and temporal convergence rates, respectively. Based on Eqs. (47) to (50), the relation between the two spatial relative errors, *i.e.*, Eq. (51), and the relation between two temporal relative errors, *i.e.*, Eq. (52), can be established. Thus, the spatial and temporal convergence rates can be found by virtue of Eqs. (51) and (52) (Ogami, 1999; Shao and Lo, 2003).

$$\frac{E_{r,s}^{\Delta x_{0,1},\Delta x_{0,2}}}{E_{r,s}^{\Delta x_{0,2},\Delta x_{0,3}}} = \frac{(\Delta x_{0,1})^{SCOV} - (\Delta x_{0,2})^{SCOV}}{(\Delta x_{0,2})^{SCOV} - (\Delta x_{0,3})^{SCOV}} = \frac{(\Delta x_{0,1})^{SCOV} - (\beta\Delta x_{0,1})^{SCOV}}{(\beta\Delta x_{0,1})^{SCOV} - (\beta^2\Delta x_{0,1})^{SCOV}} = \frac{1}{\beta^{SCOV}} \tag{51}$$

$$\frac{E_{r,t}^{\Delta t_1,\Delta t_2}}{E_{r,t}^{\Delta t_2,\Delta t_3}} = \frac{(\Delta t_1)^{TCOV} - (\Delta t_2)^{TCOV}}{(\Delta t_2)^{TCOV} - (\Delta t_3)^{TCOV}} = \frac{(\Delta t_1)^{TCOV} - (\beta\Delta t_1)^{TCOV}}{(\beta\Delta t_1)^{TCOV} - (\beta^2\Delta t_1)^{TCOV}} = \frac{1}{\beta^{TCOV}} \tag{52}$$

In addition, to investigate the numerical accuracy, the L_2 relative error norm based on the variable ϕ as shown in Eq. (53) is therefore introduced.

$$L_2(\phi) = \sqrt{\frac{\sum_{i=1}^{i=N_g}(\phi_i^{\text{simulated}} - \phi_i^{\text{exact}})^2}{\sum_{i=1}^{i=N_g}(\phi_i^{\text{exact}})^2}} \times 100\% \tag{53}$$

where $\phi^{\text{simulated}}$ and ϕ^{exact} are the simulated results and the exact solutions, respectively.

The simulated results using the standard SPH-SWEs model, which involves the Wendland kernel function and the Monaghan artificial viscosity formulation such as Eq. (B.1) in which C_α is set to be 0.5, are also shown in each test case to assess the performance of the two different SPH-SWEs models. The required CPU times of each study case are tabulated in Table 2.

5.1. Case 1: Subcritical → supercritical → subcritical → supercritical condition

The first study case is of a 1000 m long and 10 m wide rectangular channel with the incoming subcritical flow and the outgoing supercritical flow. Fig. 5 shows the profiles of the bed elevation, free surface level and critical level for this case. The flow is subcritical at the inflow boundary, then changes to the supercritical condition at the x = 300 m, returns to the subcritical condition again at x = 600 m via hydraulic jump and the flow finally changes to supercritical condition at the outflow boundary. The only required boundary condition is the water discharge of 20m^3/s specified at the inflow boundary. The Manning's roughness coefficient is 0.02 s/m$^{1/3}$.

In this study case, the initial particle spacings, namely 5 m, 10 m and 20 m, are used to calculate the spatial convergence rate through Eq. (51) while Eq. (52) gives the temporal convergence rate considering the time steps of 0.2 s, 0.4 s and 0.8 s. The spatial convergence rate is 1.93 and the temporal convergence rate is 1.11. The calculated rates of convergence in space and in time correspond to Eqs. (44) and (46), respectively. The simulated profiles of the water depth and discharge along the channel with Δx_0 = 5 m and Δt = 0.2 s are presented in Fig. 6. In Fig. 6a of the simulated profile of water depth, oscillation occurs in the vicinity of hydraulic jump using the standard SPH-SWEs model. This is not the case using the proposed model. Also, oscillations in water discharge caused by the standard SPH-SWEs model are large than those predicted from the proposed model in Fig. 6b. Furthermore, $L_2(d_w)$ and $L_2(Q)$ are calculated as 3.2% and 1.1% through Eq. (53), respectively. It can be found that the simulated results show good agreement with the exact solutions.

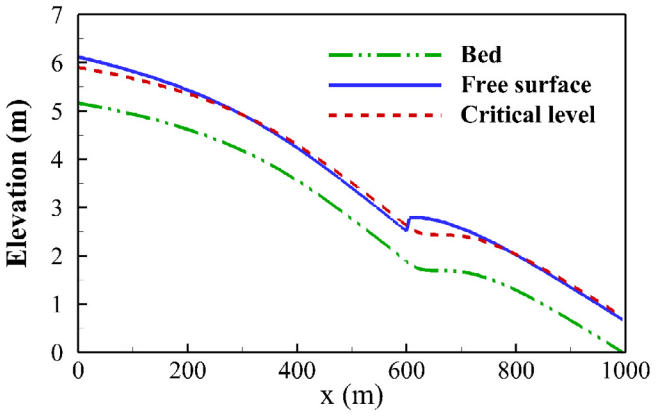

Fig. 5. Bed elevation, free surface level and critical level for case 1.

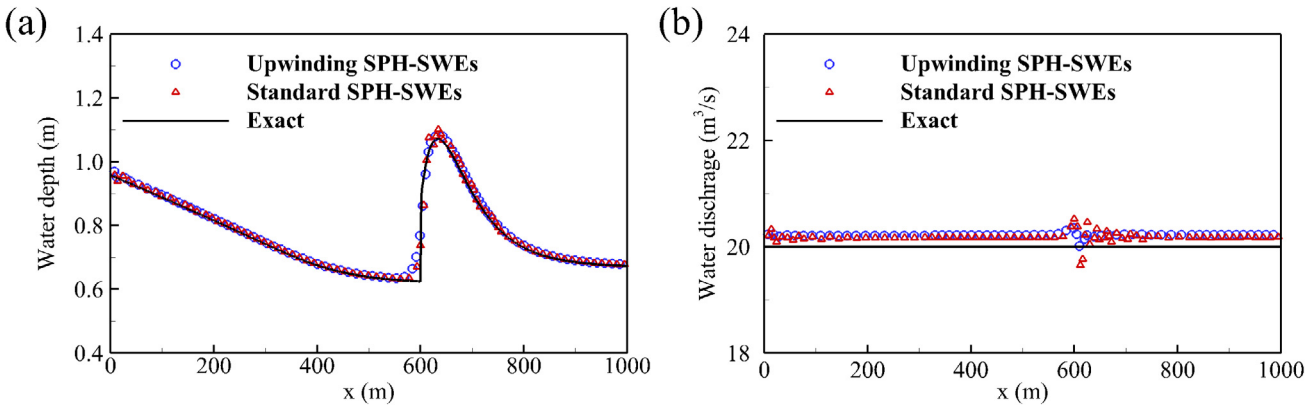

Fig. 6. The simulated profiles of (a) water depth; (b) water dischrage for case 1.

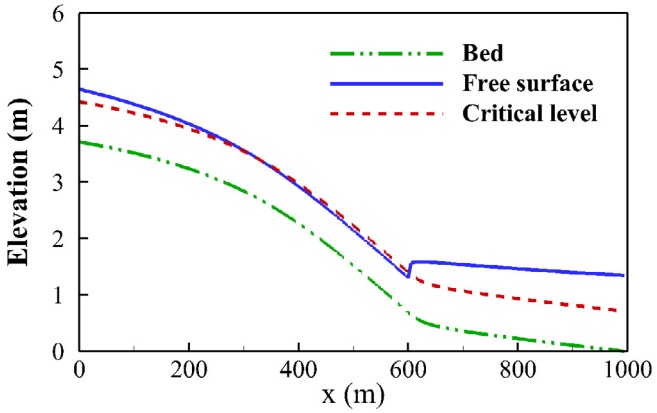

Fig. 7. Bed elevation, free surface level and critical level for case 2.

5.2. Case 2: Subcritical → supercritical → subcritical condition

A trapezoidal channel of length 1000 m, bottom width 10 m and side slope 1 is conducted as the second study case. The bed elevation, free surface level and critical level are depicted in Fig. 7. Subcritical flow starts at the inflow boundary, changing smoothly to supercritical flow at $x = 300$ m, back to subcritical flow at $x = 600$ m and the subcritical flow remains unchanged at the outflow boundary. A hydraulic jump at $x = 600$ m resulting from the bed slope turns to be milder. Owing to subcritical flows at both the in/out-flow boundaries, the inflow water discharge 20m^3/s and the outflow water depth 1.349963 m are determined to be the in/out-flow boundary conditions for this case. To describe rough channel bed, the Manning's roughness coefficient is set to be 0.02 s/m$^{1/3}$.

To discuss the spatial and temporal rates of convergence respectively, three initial particle spacings including 20 m, 10 m and 5 m and three time steps concerning 0.2 s, 0.1 s and 0.05 s are applied respectively. Through Eqs. (51) and (52), the spatial and temporal convergence rates are calculated as 2.36 and 1.12, which are consistent with Eqs. (44) and (46). In addition, Fig. 8 exhibits the simulated profiles of water depth and discharge in $\Delta x_0 = 5$ m and $\Delta t = 0.2$ s. In comparison with the exact solutions, it can be seen that the two investigated SPH-SWEs models give good prediction of the hydraulic jump in Fig. 8a while the proposed model suffers a lesser oscillation in water discharge in Fig. 8b. Eq. (53) leads to $L_2(d_w)$ of 2.1% and $L_2(Q)$ of 1.0% for the proposed model. The proposed model is capable of predicting the channel flow with the subcritical inflow and subcritical outflow conditions accurately.

5.3. Case 3: Supercritical → subcritical → supercritical condition

In the third study case, we investigate a rectangular channel flow subject to supercritical inflow and supercritical outflow conditions. The rectangular channel of length 1000 m and width 10 m has the Manning's roughness coefficient of 0.02 s/m$^{1/3}$.

Fig. 9 shows that bed elevation, free surface level and critical level for the third case. From Fig. 9, it can be seen that supercritical

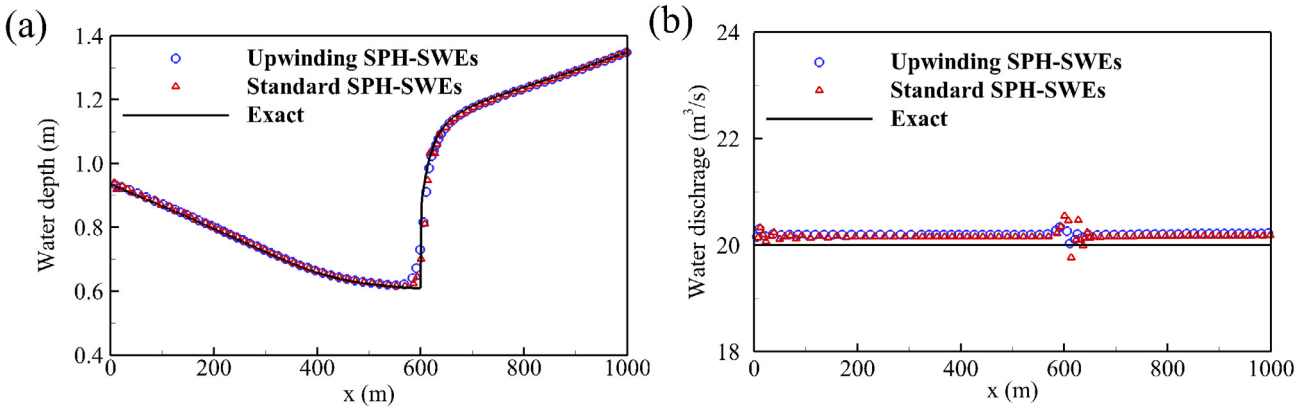

Fig. 8. The simulated profiles of (a) water depth and (b) water dischrage for case 2.

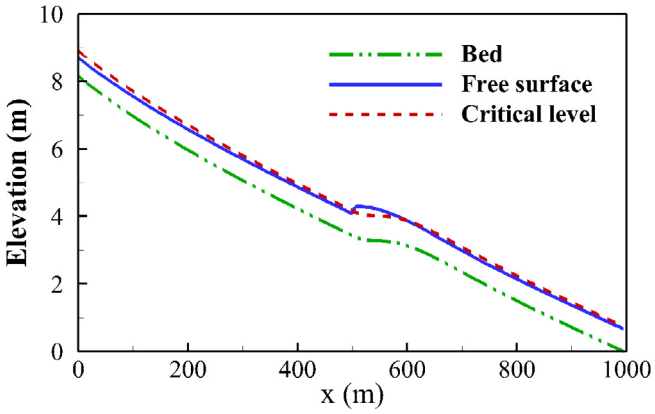

Fig. 9. Bed elevation, free surface level and critical level for case 3.

flow changes to subcritical flow at $x = 500$ m via hydraulic jump and then it returns to supercritical flow at $x = 600$ m soon. The inflow boundary conditions of water depth of the 0.543853 m and water discharge of the 20 m^3/s are given herein.

Firstly, we select the initial particle spacings of 20 m, 10 m and 5 m and the time steps of 0.2 s, 0.1 s and 0.05 s, respectively, to perform the convergence analyses in space and time using Eqs. (51) and (52), respectively. The spatial convergence rate is 0.85 while the temporal convergence rate is 1.23. Owing to the particle discretization error introduced into the formulation, the calculated spatial rate of convergence is significantly less than that shown in Eq. (44). In the following, the accuracy of the proposed model in this case is performed. Fig. 10 shows the simulated water depth and discharge at $\Delta x_0 = 5$ m and $\Delta t = 0.2$ s. The standard SPH-SWEs model overestimates the hydraulic jump peak and generates a slightly larger oscillation in water discharge. In contrast, the simulated results using the proposed model agree very well with the exact solutions in this case study. Moreover, $L_2(d_w)$ and $L_2(Q)$ for the proposed model are predicted as 2.7% and 0.4%, respectively, by means of Eq. (53).

5.4. Case 4: Supercritical → subcritical condition

The combination of the supercritical inflow and subcritical flow is taken as the fourth study case. In addition to the channels of uniform width, the proposed model is herein tested in a 1000 m long rectangular channel with varying widths. Fig. 11 shows the profile of the channel width for this case. In addition, bed elevation, free surface level and critical level for the non-uniform width channel are described in Fig. 12. The flow at the inflow boundary is supercritical, via hydraulic jump the investigated flow changes to be subcritical at $x = 500$ m. The water depth of 0.641667 m and the water discharge of 20m^3/s at the inflow boundary and the water depth of 1.125 m at the outflow boundary are prescribed. The channel has a rough bed with the Manning's roughness coefficient of 0.02 $s/m^{1/3}$.

Three initial particle sizes, namely, 20 m, 10 m and 5 m and three time steps, namely, 0.16 s, 0.08 s and 0.04 s are considered

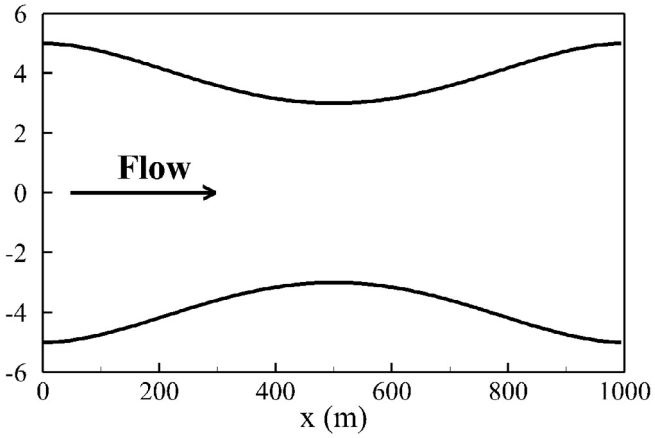

Fig. 11. The varying channel widths for case 4.

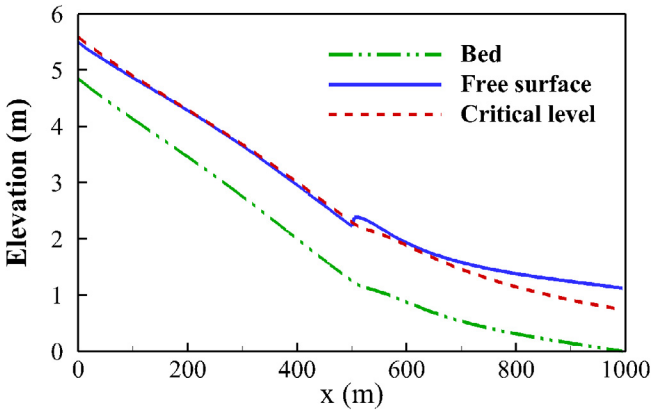

Fig. 12. Bed elevation, free surface level and critical level for case 4.

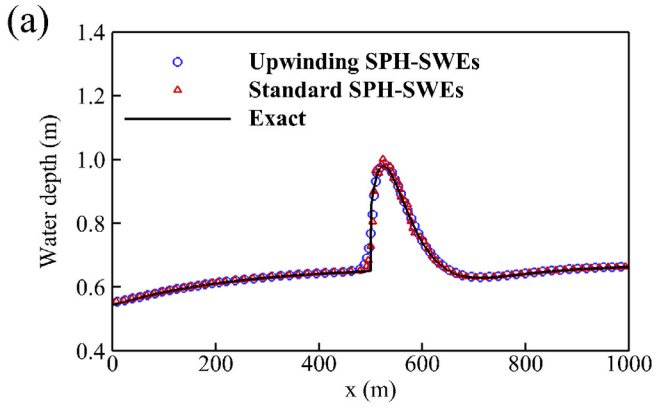

Fig. 10. The simulated profiles of (a) water depth and (b) water dischrage for case 3.

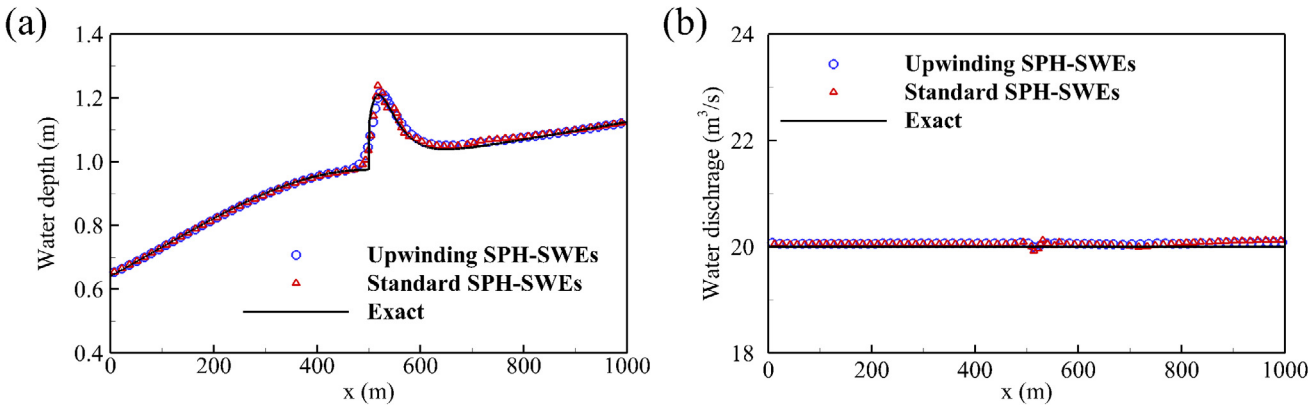

Fig. 13. The simulated profiles of (a) water depth and (b) water dischrage for case 4.

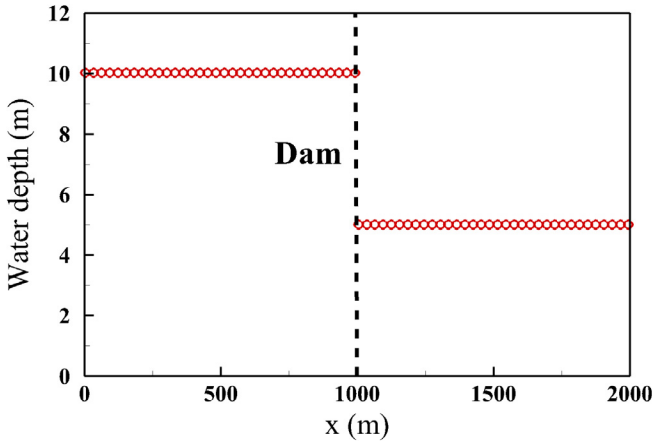

Fig. B.1. The initial profile of water depth in a dam-break flow with a wet-wet front.

to calculate the spatial and temporal rates of convergence. The spatial and temporal convergence rates calculated through Eqs. (51) and (52) are 0.94 and 1.21, respectively. It can also be found that the particle discretization has a significant effect on the calculated spatial rate of convergence in this case. Fig. 13 shows the simulated water depth and discharge profiles at $\Delta x_0 = 5$ m and $\Delta t = 0.16$ s. To compare with the exact solutions, it appears that the height of hydraulic jump is overestimated by the standard SPH-SWEs model while the proposed model can capture hydraulic jump more accurately. In addition, slightly severe oscillations in water discharge can be detected in the standard SPH-SWEs model. The predicted $L_2(d_w)$ of 1.4% and $L_2(Q)$ of 0.3% given by Eq. (53) illustrate that the proposed model can be applied to get a good prediction of the non-uniform width channel flow with supercritical inflow and subcritical outflow conditions.Fig. B.1

6. Concluding remarks

The aim of this study is to construct an upwinding kernel function in the SPH-SWEs model to capture sharp surface in open channel flows. In the proposed model, the upwinding coefficient determined at the condition of yielding the smallest numerical dispersive and dissipative errors in wave space has been shown to be able to add a proper numerical diffusion to smear steep gradient or discontinuity in free surface flows. In addition to rectangular and trapezoidal channels, uniform and non-uniform widths, non-uniform bed slope, transcritical flow and hydraulic jump, combination of four in/out-flow boundary conditions has been considered to verify the proposed model. The simulated results show good agreement with the exact solutions. To compare with the standard SPH-SWEs model, the proposed model can not only capture hydraulic jump more accurately but also suffers less oscillation problem in water discharge near hydraulic jump. Furthermore, the convergence analysis has been performed theoretically and numerically. It can be found that the calculated temporal rates of convergence are close to the theoretical rates while the calculated spatial rates of convergence are less than the theoretical rates under the particle discretization. To sum up, the present upwinding SPH-SWEs model has shown its capability to model complex transcritical open channel flows permitting the formation of hydraulic jump.

Appendix A

The process of deriving the upwinding coefficient is detailed herein. Firstly, substitution of $\alpha_r = \sum_{b=1}^{b=N,b\neq a} f_b \sin(\alpha l_b \Delta)$ and $\alpha_i = \sum_{b=1}^{b=N} f_b \cos(\alpha l_b \Delta)$ into Eq. (14) yields

$$\begin{aligned} E &= E_r + E_i \\ &= \int_0^{\pi/2} \Big| \sum_{b=1}^{b=N,b\neq a} f_b \sin(kl_b)\Delta - k \Big|^2 \mathrm{d}k \\ &\quad + \lambda \int_0^{\pi/2} \Big| \sum_{b=1}^{b=N} f_b \cos(kl_b)\Delta - e^{-\ln 2\cdot\left(\frac{k-\pi}{\sigma}\right)^2} \Big|^2 \mathrm{d}k \end{aligned} \tag{A.1}$$

To differentiate Eq. (A.1) by f_{ct}, where $ct = 1$ *to* N *but* $ct \neq a$, the terms of $\partial E_r/\partial f_{ct}$ and $\partial E_i/\partial f_{ct}$ can thus be given as Eqs. (A.2) and (A.3), resectively.

$$\begin{aligned} \frac{\partial E_r}{\partial f_{ct}} &= \int_0^{\pi/2} \frac{\partial \left(\sum_{b=1}^{b=N,b\neq a} f_b \sin(kl_b)\Delta - k \right)^2}{\partial f_{ct}} \mathrm{d}k \\ &= \int_0^{\pi/2} 2 \left(\sum_{b=1}^{b=N,b\neq a} f_b \sin(kl_b)\Delta - k \right) \sin(kl_{ct})\Delta \mathrm{d}k \\ &= \Delta \left[\sum_{b=1}^{b=N,b\neq a} f_b \Delta \int_0^{\pi/2} 2\sin(kl_b)\sin(kl_{ct})\mathrm{d}k - 2\int_0^{\pi/2} k\sin(kl_{ct})\mathrm{d}k \right] \\ &= \Delta \left[\sum_{b=1}^{b=N,b\neq a} f_b \Delta \left(\int_0^{\pi/2} (\cos(l_b - l_{ct})k - \cos(l_b + l_{ct})k)\mathrm{d}k \right) + S_r \right] \\ &= \Delta \left[\sum_{b=1}^{b=N,b\neq a} f_b \left(\frac{\sin(l_b - l_{ct})\pi/2}{l_b - l_{ct}} - \frac{\sin(l_b + l_{ct})\pi/2}{l_b + l_{ct}} \right) \Delta + S_r \right] \end{aligned} \tag{A.2}$$

$$\frac{\partial E_i}{\partial f_{ct}} = \int_0^{\pi/2} \frac{\partial\left(\sum_{b=1}^{b=N} f_b \cos(kl_b)\Delta - e^{-\ln 2\cdot\left(\frac{k-\pi}{\sigma}\right)^2}\right)^2}{\partial f_{ct}} dk$$
$$= \int_0^{\pi/2} 2\left(\sum_{b=1}^{b=N} f_b \cos(kl_b)\Delta - e^{-\ln 2\cdot\left(\frac{k-\pi}{\sigma}\right)^2}\right)\cos(kl_{ct})\Delta dk$$
$$= \Delta\left[\sum_{b=1}^{b=N} f_b \Delta \int_0^{\pi/2} 2\cos(kl_b)\cos(kl_{ct})dk - 2\int_0^{\pi/2} e^{-\ln 2\cdot\left(\frac{k-\pi}{\sigma}\right)^2}\cos(kl_{ct})dk\right]$$
$$= \Delta\left[\sum_{b=1}^{b=N} f_b \Delta \int_0^{\pi/2} (\cos(l_b - l_{ct})k + \cos(l_b + l_{ct})k)dk - 2\int_0^{\pi/2} e^{-\ln 2\cdot\left(\frac{k-\pi}{\sigma}\right)^2}\cos(kl_{ct})dk\right]$$
$$= \Delta\left[\sum_{b=1}^{b=N} f_b \left(\frac{\sin(l_b - l_{ct})\pi/2}{l_b - l_{ct}} + \frac{\sin(l_b + l_{ct})\pi/2}{l_b + l_{ct}}\right)\Delta + S_i\right] \tag{A.3}$$

Using the definition of $f_a = -\sum_{b=1}^{b=N,b\neq a} f_b$ together with Eqs. (A.2) and (A.3), Eq. (15) becomes as

$$\frac{\partial E}{\partial f_{ct}} = \frac{\partial E_r}{\partial f_{ct}} + \lambda\frac{\partial E_i}{\partial f_{ct}} = \sum_{b=1}^{b=N,b\neq a} f_b\left[\frac{\sin(l_b - l_{ct})\pi/2}{l_b - l_{ct}} - \frac{\sin(l_b + l_{ct})\pi/2}{l_b + l_{ct}}\right]\Delta + S_r$$
$$+\lambda\sum_{b=1}^{b=N} f_b\left[\frac{\sin(l_b - l_{ct})\pi/2}{l_b - l_{ct}} + \frac{\sin(l_b + l_{ct})\pi/2}{l_b + l_{ct}}\right]\Delta + \lambda S_i$$
$$= \sum_{b=1}^{b=N,b\neq a} f_b C_b\Delta + f_a C_a\Delta + (S_r + \lambda S_i) \tag{A.4}$$
$$= \sum_{b=1}^{b=N,b\neq a} f_b C_b\Delta - \sum_{b=1}^{b=N,b\neq a} f_b C_a\Delta + (S_r + \lambda S_i)$$
$$= \sum_{b=1}^{b=N,b\neq a} f_b(C_b - C_a)\Delta + (S_r + \lambda S_i) = 0$$

In the above,

$$C_a = \lambda\Delta\left[\frac{\sin((l_a - l_{ct})\pi/2)}{l_a - l_{ct}} + \frac{\sin((l_a + l_{ct})\pi/2)}{l_a + l_{ct}}\right],$$

$$C_b = \Delta\left[(\lambda+1)\frac{\sin((l_b - l_{ct})\pi/2)}{l_b - l_{ct}} + (\lambda-1)\frac{\sin((l_b + l_{ct})\pi/2)}{l_b + l_{ct}}\right],$$

$$S_r = -2\int_0^{\pi/2} k\sin(l_{ct}k)dk,$$

$$S_i = -2\int_0^{\pi/2} \cos(l_{ct}k)\cdot e^{-\ln 2\cdot\left(\frac{k-\pi}{\sigma}\right)^2} dk.$$

Because of $f_b = -m_b(\omega^a_{ab,x} + \tau_a u_a \omega^a_{ab,xx})/A_a$, Eq. (A.4) can be expressed as Eq. (A.5) and finally simple algebraic manipulations can lead to the upwinding coefficient such as Eq. (16).

$$\sum_{b=1}^{b=N,b\neq a} [-m_b(\omega^a_{ab,x} + \tau_a u_a \omega^a_{ab,xx})/A_a](C_b - C_a)\Delta + (S_r + \lambda S_i) = 0 \tag{A.5}$$

Appendix B

One of the attractive advantages in SPH is that the wet-dry interface can be automatically described without a special treatment. Hence, the dam break flow has become a benchmark problem to exhibit the ability of SPH. Herein, the dam break flow with a wet-wet front is used to assess the performance of different values of the weighted parameter λ in the proposed upwinding SPH-SWEs model against the exact solutions (Stoker, 1992) and the numerical solutions (the standard SPH-SWEs model). In the standard SPH-SWEs model, the artificial viscosity formulation such as Eq. (B.1) is applied in this study (Monaghan, 1985; De Leffe et al., 2010).

$$\begin{cases} \prod_{ab} = -C_\alpha \sum_{b=1}^{b=N} V_b \frac{\bar{A}\cdot\bar{c}\cdot\bar{h}\cdot(u_{ab}\cdot x_{ab})}{r_{ab}^2}\bar{\omega}_x & u_{ab}\cdot x_{ab} < 0 \\ \prod_{ab} = 0 & u_{ab}\cdot x_{ab} \geqslant 0 \end{cases} \tag{B.1}$$

where V_b is the volume of particle b, $\bar{\omega}_x$ is the average of the first derivative of the symmetric kernel function, $u_{ab} = u_a - u_b$, $x_{ab} = x_a - x_b$, $\bar{A} = 0.5(A_a + A_b)$, $\bar{c} = 0.5(c_a + c_b)$, $\bar{h} = 0.5(h_a + h_b)$, $r_{ab} = |x_a - x_b|$ and C_α is the parameter ($0 \leqslant C_\alpha \leqslant 1$).

In this case, a dam break flow with a wet-wet front on a horizontal and frictionless bottom is discussed. Fig. B.1 shows the initial profile of water depth of this case. A water column of 10 m height and 1000 m length at the upstream side of the dam and a water column of 5 m height and 1000 m length at the downstream side of the dam are adopted to preserve mass in the computational domain. Herein, the weighted parameter λ of 1.0, 0.5 and 0.3 and the parameter C_α of 0.5, 0.7 and 1.0 are considered, respectively. The initial particle spacing at the upstream side is set to be 5 m while the one at the downstream side is specified to be 10 m. Hence, the total number of particles such as 300 is involved in simulation. The initial smoothing length is assumed to be twice the length of the initial particle spacing, *i.e.*, $h = 2\Delta x_0$. In addition, the time step of 0.008 s is chosen.

Figs. B.2 and B.3 exhibit the simulated profiles of water depth and velocity at t = 60 s, respectively. From Fig. B.2a to c and Fig. B.3a to c, it can be seen that the oscillations in water depth and velocity near the bore (in the vicinity of x = 1500 m) will be suppressed as the value of the weighted parameter λ is decreased because the weighted parameter λ controls the weights between the dispersion error (E_r) and dissipation error (E_i) over finite particles. A smaller value of the weighted parameter λ, *i.e.*, large weight on the dispersion error, can produce smoother simulated profiles of water depth and velocity in this case. On the other hand, the parameter C_α dominates the magnitude of the artificial viscous force in the standard SPH-SWEs model. In Fig. B.2d to f and Fig. B.3d to f, the larger value of the parameter C_α of 1.0 can eliminate large portion of the oscillations in water depth and velocity, especially near the bore. However, as a comparison of the proposed upwinding SPH-SWEs model (Figs. B.2c and B.3c), in Fig. B.2. f and Fig. B.3 f, the reflective waves in water depth and velocity are generated in the expansion region (in the vicinity of x = 670 m) and less oscillations in water depth and velocity still exist near the bore. On the whole, the proposed upwinding SPH-SWEs model yields a better simulated result against the exact solution.

Appendix C

The slopes and exact solutions for the four study cases are given herein following the work of MacDonald et al. (1995).

Study case 1

The slope of the uniform rectangular channel in the first study case is expressed as follows:

$$S_0(x) = \left(1 - \frac{Q^2}{gB^2 d_w(x)}\right)d'_w(x) + Q^2 n^2 \frac{(2d_w(x) + B)^{4/3}}{(Bd_w(x))^{10/3}} \tag{C.1}$$

where the water discharge $Q = 20\text{m}^3/\text{s}$, the bottom width $B = 10$ m, the Manning's roughness coefficient $n = 0.02$, the exact solution of water depth $d_w(x)$ is given as below and $d'_w(x)$ is its first derivative with respect to x.

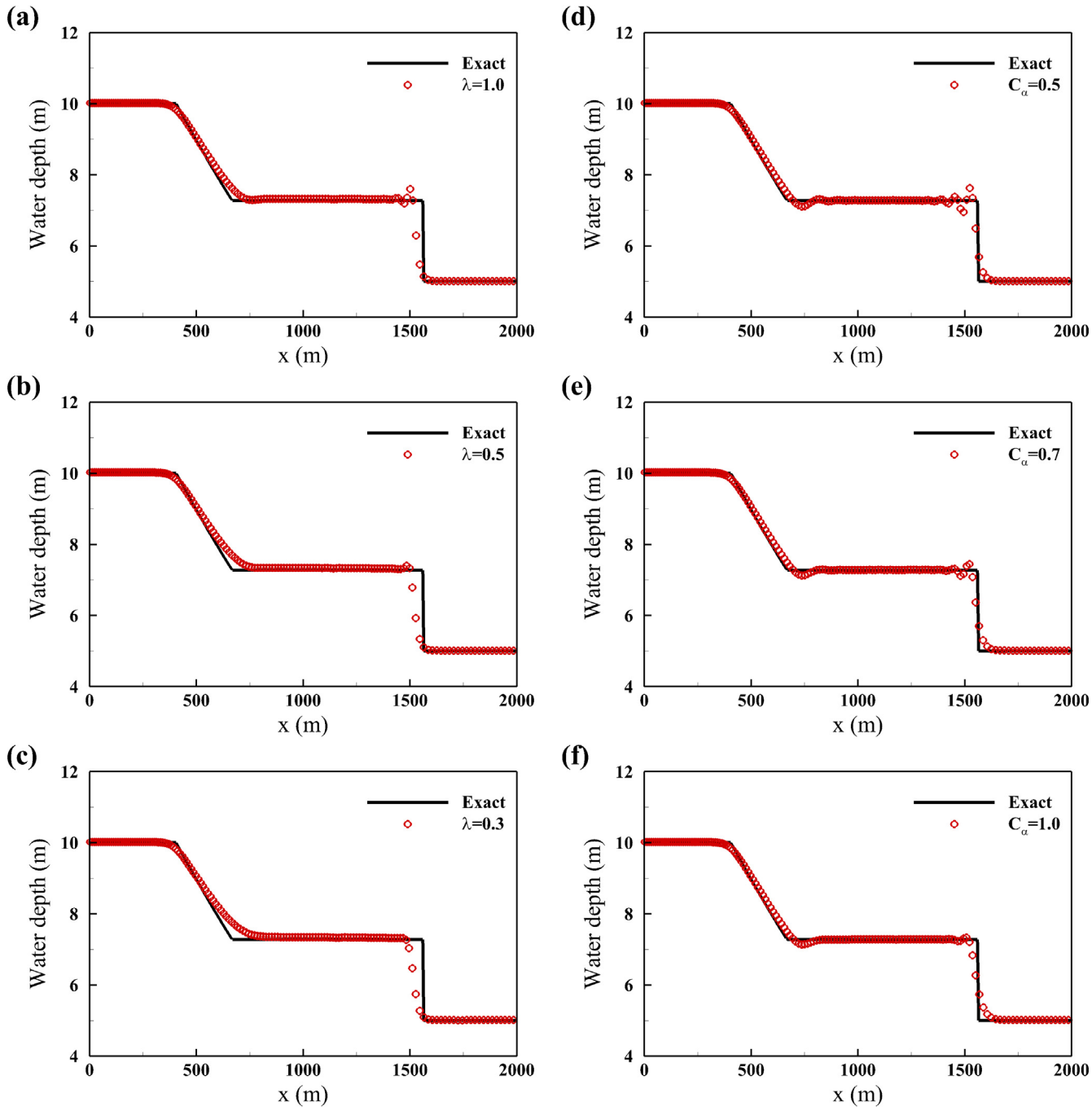

Fig. B.2. The profiles of water depth in a dam-break flow with a wet-wet front, (a)–(c) from the upwinding SPH-SWEs model and (d)–(f) from the standard SPH-SWEs model.

$$d_w(x)=\begin{cases}\left(\frac{4}{g}\right)^{1/3}\left(1-\tanh\left(\frac{x}{1000}-\frac{3}{10}\right)\right) & 0\leqslant x\leqslant 300\\ \left(\frac{4}{g}\right)^{1/3}\left[1-\frac{1}{6}\tanh\left(6\left(\frac{x}{1000}-\frac{3}{10}\right)\right)\right] & 300<x\leqslant 600\\ \hat{d}_w(x) & 600<x\leqslant 1000\end{cases} \tag{C.2}$$

In the above,

$$\hat{d}_w(x)=\left(\frac{4}{g}\right)^{1/3}\left[k_1+k_2\exp\left(-10\left(\frac{x}{1000}-\frac{3}{5}\right)\right)+k_3\exp\left(-20\left(\frac{x}{1000}-\frac{3}{5}\right)\right)+k_4\exp\left(-30\left(\frac{x}{1000}-\frac{3}{5}\right)\right)\right] \tag{C.3}$$

where $k_1 = 0.900000$, $k_2 = 0.382537$, $k_3 = 2.131437$ and $k_4 = -2.237556$.

Study case 2

In the second study case, the slope of the uniform trapezoidal channel is written as

$$S_0(x)=\left[1-\frac{Q^2(B+2d_w(x)z)}{g(B+d_w(x)z)^3d(x)^3}\right]d'_w(x)+\frac{Q^2n^2(B+2d_w(x)\sqrt{1+z^2})^{4/3}}{(B+d_w(x)z)^{10/3}d(x)^{10/3}} \tag{C.4}$$

where the water discharge $Q = 20\text{m}^3/\text{s}$, the bottom width $B = 10$ m, the side slope $z = 1$ the Manning's roughness coefficient $n = 0.02$, the exact solution of water depth $d_w(x)$ is given as

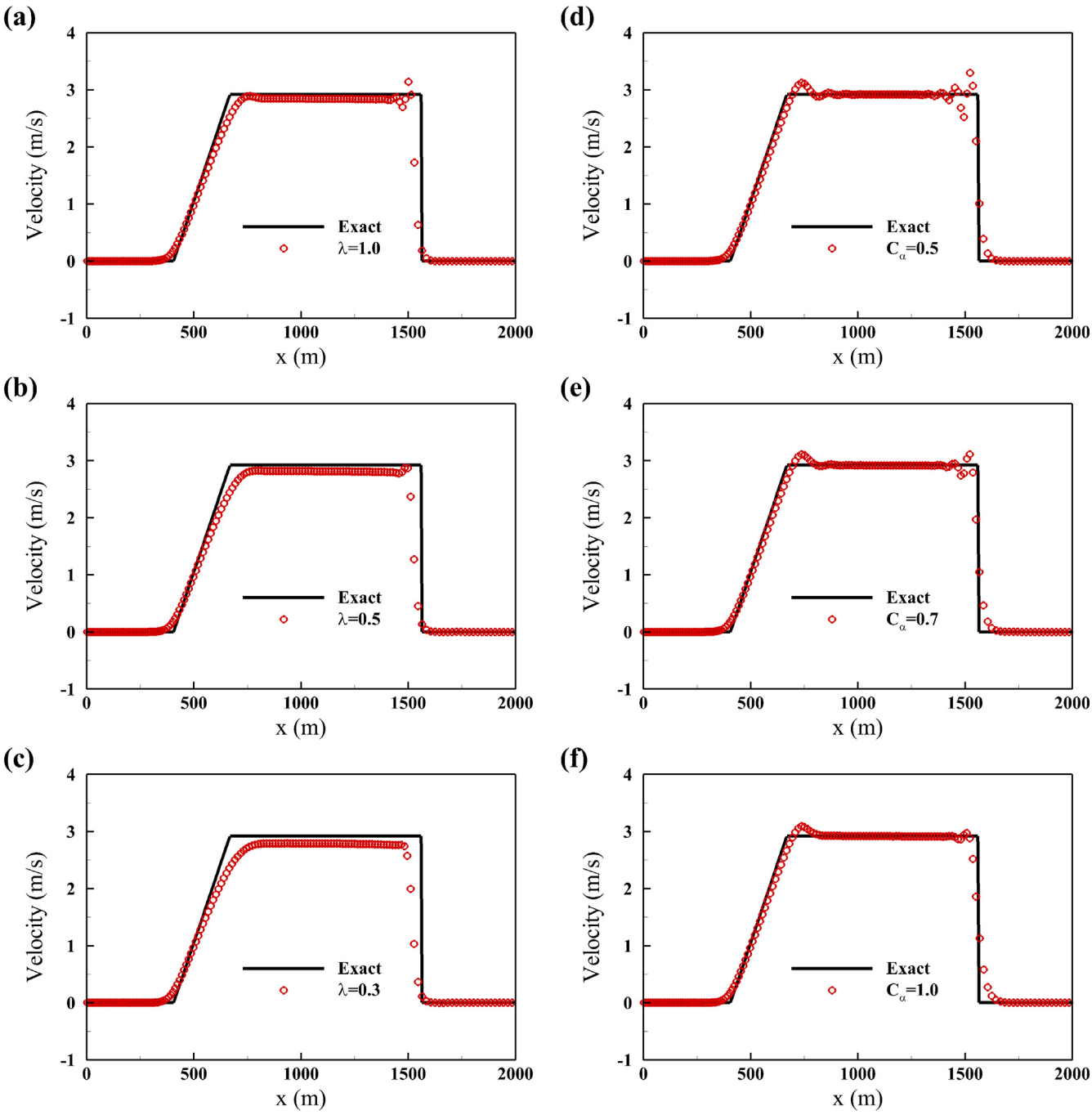

Fig. B.3. The profiles of velocity in a dam-break flow with a wet-wet front, (a)–(c) from the upwinding SPH-SWEs model and (d)–(f) from the standard SPH-SWEs model.

$$d_w(x) = \begin{cases} 0.723449\left(1 - \tanh\left(\frac{x}{1000} - \frac{3}{10}\right)\right) & 0 \leqslant x \leqslant 300 \\ 0.723449\left[1 - \frac{1}{6}\tanh\left(6\left(\frac{x}{1000} - \frac{3}{10}\right)\right)\right] & 300 < x \leqslant 600 \\ \hat{d}_w(x) & 600 < x \leqslant 1000 \end{cases} \tag{C.5}$$

In the above,

$$\begin{aligned} \hat{d}_w(x) = {} & k_1 + k_2 \exp\left(-20\left(\frac{x}{1000} - \frac{3}{5}\right)\right) \\ & + k_3 \exp\left(-40\left(\frac{x}{1000} - \frac{3}{5}\right)\right) \\ & + k_4 \exp\left(-60\left(\frac{x}{1000} - \frac{3}{5}\right)\right) + k_5 \exp\left(\frac{x}{1000} - 1\right) \end{aligned} \tag{C.6}$$

where k_1 = 0.750000, k_2 = -0.111051, k_3 = 0.026876, k4 = -0.217567 and k_5 = 0.600000.

Study case 3

For the third study case, the slope of the uniform rectangular channel is given by

$$S_0(x) = \left(1 - \frac{Q^2}{gB^2 d_w(x)}\right) d_x'(x) + Q^2 n^2 \frac{(2d_w(x) + B)^{4/3}}{(B d_w(x))^{10/3}} \tag{C.7}$$

where the water discharge $Q = 20\text{m}^3/\text{s}$, the bottom width B = 10 m, the Manning's roughness coefficient n = 0.02, the exact solution of water depth $d_w(x)$ is given as

$$d_w(x) = \begin{cases} \left(\frac{4}{g}\right)^{1/3}\left(\frac{9}{10} - \frac{1}{6}\exp\left(\frac{-x}{250}\right)\right) & 0 \leqslant x \leqslant 500 \\ \hat{d}_w(x) & 500 < x \leqslant 1000 \end{cases} \quad (C.8)$$

In the above,

$$\hat{d}_w(x) = \left(\frac{4}{g}\right)^{1/3}\left[k_1 + k_2\exp\left(-10\left(\frac{x}{1000} - \frac{1}{2}\right)\right) + k_3\exp\left(-20\left(\frac{x}{1000} - \frac{1}{2}\right)\right) + k_4\exp\left(-30\left(\frac{x}{1000} - \frac{1}{2}\right)\right)\right] \quad (C.9)$$

where $k_1 = 0.900000$, $k_2 = -0.901807$, $k_3 = 4.373858$ and $k_4 = -3.238569$.

Study case 4

For the non-uniform rectangular channel in the fourth study case, the slope is expressed as

$$S_0(x) = \left(1 - \frac{Q^2}{gB(x)^2 d_w(x)^3}\right)d_w'(x) + \frac{Q^2 n^2 (B(x) + 2d_w(x))^{4/3}}{(B(x)d_w(x))^{10/3}} - \frac{Q^2 B'(x)}{gB(x)^3 d_w(x)^2} \quad (C.10)$$

where the water discharge $Q = 20\text{m}^3/\text{s}$, the Manning's roughness coefficient $n = 0.02$, the varying channel width $B(x)$ and the exact solution of water depth to $d_w(x)$ are given below respectively.

$$B(x) = 10 - 64\left(\left(\frac{x}{1000}\right)^2 - 2\left(\frac{x}{1000}\right)^3 + \left(\frac{x}{1000}\right)^4\right) \quad (C.11)$$

and

$$\hat{d}_w(x) = \begin{cases} -\frac{1}{40} + \frac{1}{1+2\left(\frac{x}{1000} - \frac{1}{2}\right)^2} & 0 \leqslant x \leqslant 500 \\ \hat{d}_w(x) & 500 < x \leqslant 1000 \end{cases} \quad (C.12)$$

In the above,

$$\hat{d}_w(x) = k_1 + k_2\exp\left(-30\left(\frac{x}{1000} - \frac{1}{2}\right)\right) + k_3\exp\left(-60\left(\frac{x}{1000} - \frac{1}{2}\right)\right) + k_4\exp\left(-90\left(\frac{x}{1000} - \frac{1}{2}\right)\right) + k_5\exp\left(\frac{x}{4000} - \frac{1}{4}\right) \quad (C.13)$$

where $k_1 = 0.000000$, $k_2 = 0.769035$, $k_3 = -0.755596$, $k_4 = 0.106813$ and $k_5 = 1.125000$

References

Alcrudo, F., Garcia-Navarro, P., Saviron, J.M., 1992. Flux difference splitting for 1d open channel flow equations. Int. J. Numer. Methods Fl. 14 (9), 1009–1018.

Anderson, B.G., Rutherfurd, I.D., Western, A.W., 2006. An analysis of the influence of riparian vegetation on the propagation of flood waves. Environ. Modell. Softw. 21 (9), 1290–1296.

Aristodemo, F., Marrone, S., Federico, I., 2015. SPH modelling of plane jets into water bodies through an inflow/outflow. Ocean. Eng. 105, 160–175.

Ata, R., Soulaimani, A., 2005. A stabilized SPH method for inviscid shallow water flows. Int. J. Numer. Methods Fl. 47 (2), 139–159.

Bonet, J., Lok, T.S.L., 1999. Variational and momentum preservation aspects of Smooth Particle Hydrodynamic formulations. Comput. Methods Appl. M 180 (1–2), 97–115.

Brooks, A.N., Hughes, T.J.R., 1982. Streamline upwind Petrov-Galerkin formulations for convection dominated flows with particular emphasis on the incompressible Navier-Stokes equations. Comput. Methods Appl. M 32 (1–3), 199–259.

Chang, T.J., Chang, K.H., 2013. SPH modeling of one-dimensional nonrectangular and nonprismatic channel flows with open boundaries. J. Hydraul. Eng. ASCE 139 (11), 1142–1149.

Chang, T.J., Kao, H.M., Chang, K.H., Hsu, M.H., 2011. Numerical simulation of shallow-water dam break flows in open channels using smoothed particle hydrodynamics. J. Hydrol. 408 (1–2), 78–90.

Chen, R., Shao, S., Liu, X., Zhou, X., 2015. Applications of shallow water SPH model in mountainous rivers. J. Appl. Fluid Mech. 8 (4), 863–870.

Cheong, C., Lee, S., 2001. Grid-optimized dispersion-relation-preserving schemes on general geometries for computational aeroacoustics. J. Comput. Phys. 174 (1), 248–276.

De Leffe, M., Le Touze, D., Alessandrini, B., 2010. SPH modeling of shallow-water coastal flows. J. Hydraul. Res. 48, 118–125.

Diaz, M.J.C., Ferndndez-Nieto, E.D., Ferreiro, A.M., 2008. Sediment transport models in Shallow Water equations and numerical approach by high order finite volume methods. Comput. Fluids 37 (3), 299–316.

Federico, I., Marrone, S., Colagrossi, A., Aristodemo, F., Antuono, M., 2012. Simulating 2D open-channel flow through an SPH model. Eur. J. Mech. B Fluid 34, 35–46.

Garcia-Navarro, P., Saviron, J.M., 1992. McCormack method for the numerical-simulation of one-dimensional discontinuous unsteady open channel flow. J. Hydraul. Res. 30 (1), 95–105.

Gomez-Gesteira, M., Rogers, B.D., Dalrymple, R.A., Crespo, A.J.C., 2010. State-of-the-art of classical SPH for free-surface flows. J. Hydraul. Res 48(SI), 6–27.

Hernquist, L., Katz, N., 1989. TREESPH: a unification of sph with the hierarchical tree method. Astrophys. J. Suppl. Ser. 70 (2), 419–446.

Hsu, M.H., Fu, J.C., Liu, W.C., 2006. Dynamic routing model with real-time roughness updating for flood forecasting. J. Hydraul. Eng. ASCE 132 (6), 605–619.

Huang, C., Sheu, T.W.H., 2012. Development of an upwinding particle interaction kernel for simulating incompressible Navier-Stokes equations. Numer. Methods Partial Differ. Equ. 28 (5), 1574–1597.

Jadhav, R.S., Buchberger, S.G., 1995. Effects of vegetation on flow through free water surface wetlands. Ecol. Eng. 5 (4), 481–496.

Kao, H.M., Chang, T.J., 2012. Numerical modeling of dambreak-induced flood and inundation using smoothed particle hydrodynamics. J. Hydrol. 448, 232–244.

Katopodes, N.D., 1984. A dissipative Galerkin scheme for open-channel flow. J. Hydraul. Eng. ASCE 110 (4), 450–466.

Li, Y.G., 1997. Wavenumber-extended high-order upwind-biased finite-difference schemes for convective scalar transport. J. Comput. Phys. 133 (2), 235–255.

Lin, G.F., Lai, J.S., Guo, W.D., 2003. Finite-volume component-wise TVD schemes for 2D shallow water equations. Adv. Water. Resour. 26 (8), 861–873.

Liu, G.R., Liu, M.B., 2003. Smoothed Particle Hydrodynamics: A Meshfree Particle Method. World Scientific, Singapore.

MacDonald, I., Baines, M.J., Nichols, N.K., Samuels, P.G., 1995. Comparisons of some steady state Saint-Venant solvers for some test problems with analytic solutions. Numerical analysis reports 2/95.

Monaghan, J.J., 1985. Particle methods for hydrodynamics. Comput. Phys. Rep. 3, 71–124.

Monaghan, J.J., 2005. Smoothed particle hydrodynamics. Rep. Prog. Phys. 68 (8), 1703–1759.

Ogami, Y., 1999. A pure Lagrangian method for unsteady compressible viscous flow. Comput. Fluid. Dyn. J. 8 (3), 383–392.

Papanicolaou, A.N., Bdour, A., Wicklein, E., 2004. One-dimensional hydrodynamic/sediment transport model applicable to steep mountain streams. J. Hydraul. Res. 42 (4), 357–375.

Quinlan, N.J., Basa, M., Lastiwka, M., 2006. Truncation error in mesh-free particle methods. Int. J. Numer. Methods Eng. 66 (13), 2064–2085.

Randles, P.W., Libersky, L.D., 1996. Smoothed particle hydrodynamics: some recent improvements and applications. Comput. Method. Appl. Mech. 139 (1–4), 375–408.

Rodriguez-Paz, M., Bonet, J., 2005. A corrected smooth particle hydrodynamics formulation of the shallow-water equations. Comput. Struct. 83 (17–18), 1396–1410.

Shao, S.D., Lo, E.Y.M., 2003. Incompressible SPH method for simulating Newtonian and non-Newtonian flows with a free surface. Adv. Water. Resour. 26 (7), 787–800.

Stoker, J.J., 1992. Water Waves: The Mathematical Theory With Applications. Wiley-Interscience.

Sturm, T.W., 2010. Open Channel Hydraulics. McGraw-Hill, New York.

Szymkiewicz, R., 1991. Finite-element method for the solution of the Saint Venant equations in an open channel network. J. Hydrol. 122 (1–4), 275–287.

Tam, C.K.W., Webb, J.C., 1993. Dispersion-relation-preserving finite-difference schemes for computational acoustics. J. Comput. Phys. 107 (2), 262–281.

Vacondio, R., Rogers, B.D., Stansby, P.K., 2012a. Smoothed particle hydrodynamics: approximate zero-consistent 2-D boundary conditions and still shallow-water tests. Int. J. Numer. Methods Fluids 69 (1), 226–253.

Vacondio, R., Rogers, B.D., Stansby, P.K., 2012b. Accurate particle splitting for smoothed particle hydrodynamics in shallow water with shock capturing. Int. J. Numer. Methods Fluids 69 (8), 1377–1410.

Vacondio, R., Rogers, B.D., Stansby, P.K., Mignosa, P., 2013. A correction for balancing discontinuous bed slopes in two-dimensional smoothed particle hydrodynamics shallow water modeling. Int. J. Numer. Methods Fluids 71, 850–872.

Violeau, D., 2012. Fluid Mechanics and the SPH Method: Theory and Applications. Oxford University Press, United Kingdom.

Wang, Z., Shen, H.T., 1999. Lagrangian simulation of one-dimensional dam-break flow. J. Hydraul. Eng. ASCE 125 (11), 1217–1220.

Xia, X., Liang, Q., Pastor, M., Zou, W., Zhuang, Y.F., 2013. Balancing the source terms in a SPH model for solving the shallow water equations. Adv. Water. Resour. 59, 25–38.

Ying, X.Y., Khan, A.A., Wang, S.S.Y., 2004. Upwind conservative scheme for the Saint Venant equations. J. Hydraul. Eng. ASCE 130 (10), 977–987.